Article

Not peer-reviewed version

Design and Evaluation of Indole-Based Schiff Bases as α-Glucosidase Inhibitors: CNN-Enhanced Docking, MD Simulations, ADMET Profiling and SAR Analysis

Seema K. Bhagwat , Sachin V. Patil , Abraham Vidal-Limon , J. Oscar C. Jimenez-Halla , Balasaheb K. Ghotekar , Vivek D. Bobade , Irving David Pérez-Landa , Enrique Delgado-Alvarado , Fabiola Hernandez-Rosas * , Tushar Janardan Pawar *

Posted Date: 6 August 2025

doi: 10.20944/preprints202508.0415.v1

Keywords: α-glucosidase inhibition; Schiff base derivatives; indole; CNN-based docking; molecular dynamics; ADMET profiling; type 2 diabetes mellitus

 doi:10.20944/preprints202508.0415.v1

Article

Design and Evaluation of Indole-Based Schiff Bases as α-Glucosidase Inhibitors: CNN-Enhanced Docking, MD Simulations, ADMET Profiling and SAR Analysis

Seema K. Bhagwat [1], Sachin V. Patil [1], Abraham Vidal-Limon [2], J. Oscar C. Jimenez-Halla [3], Balasaheb K. Ghotekar [1], Vivek D. Bobade [1], Irving David Perez-Landa [4], Enrique Delgado-Alvarado [5], Fabiola Hernandez-Rosas [6,7,*] and Tushar Janardan Pawar [2,*]

[1] Department of Chemistry, Research Centre HPT Arts and RYK Science College (Affiliated to S. P. Pune University), Nashik 422005, Maharashtra, India

[2] Red de Estudios Moleculares Avanzados, Instituto de Ecología, A. C., Carretera Antigua a Coatepec 351, 91073 Xalapa, Veracruz, México

[3] Departamento de Química, División de Ciencias Naturales y Exactas, Universidad de Guanajuato, Noria Alta S/N, 36050 Guanajuato, Guanajuato, México

[4] Tecnológico Nacional de México/Instituto Tecnológico de Boca del Río, Carretera Veracruz-Córdoba 12, Boca del Río, Veracruz 94290, Mexico

[5] Micro and Nanotechnology Research Center, Universidad Veracruzana, Blvd. Av. Ruiz Cortines No. 455 Fracc. Costa Verde, Boca del Río, Veracruz 94294, México

[6] Centro de Investigación, Universidad Anáhuac Querétaro, El Marqués, Querétaro 76246, México

[7] Facultad de Química, Universidad Autónoma de Querétaro, Querétaro 76010, México.

* Correspondence: fabiola.hernandezro@anahuac.mx (F.H.-R.); tushar.janardan@inecol.mx (T.J.P.)

Abstract

Type 2 diabetes mellitus (T2DM) remains a global health challenge, prompting the development of novel α-glucosidase inhibitors (AGIs) to regulate postprandial hyperglycemia. This study reports the design, synthesis, and evaluation of indole-based Schiff base derivatives (**4a–4j**) bearing a fixed methoxy group at the C_5 position. This substitution was strategically introduced to enhance lipophilicity, electronic delocalization, and π-stacking within the enzyme active site. Among the series, compound **4g** (3-bromophenyl) exhibited the highest inhibitory activity (IC_{50} = 10.89 μM), outperforming the clinical reference acarbose (IC_{50} = 48.95 μM). Mechanistic support from Density Functional Theory (DFT), molecular electrostatic potential (MEP) mapping, molecular dynamics simulations, and CNN-based docking revealed that 4g engages in stable hydrogen bonding and π–π interactions with key residues (Asp327, Asp542, Phe649). In silico ADMET predictions indicated favorable pharmacokinetic properties. Together, these results establish C_5–methoxy substitution as a viable strategy to enhance α-glucosidase inhibition in indole-based scaffolds.

Keywords: α-glucosidase inhibition; Schiff base derivatives; indole; CNN-based docking; molecular dynamics; ADMET profiling; type 2 diabetes mellitus

1. Introduction

Type 2 diabetes mellitus (T2DM) has emerged as a global epidemic, with significant health and economic consequences. Characterized by chronic hyperglycemia due to insulin resistance or inadequate insulin secretion, T2DM affects millions worldwide [1,2]. According to the International Diabetes Federation, the global prevalence of diabetes is projected to rise to 783 million by 2045, underscoring the urgent need for novel and effective therapeutic interventions [3,4]. Regulating

 doi:10.20944/preprints202508.0415.v1

postprandial blood glucose levels is a key strategy in T2DM management, as persistent hyperglycemia contributes to complications such as neuropathy, nephropathy, retinopathy, and cardiovascular diseases [4,5]. Among various therapeutic approaches, targeting carbohydrate-digesting enzymes, particularly α-glucosidase, has gained prominence as an effective means to delay glucose absorption and control postprandial glucose spikes [6–10].

α-Glucosidase inhibitors (AGIs), such as acarbose, voglibose, and miglitol, have been widely utilized in clinical practice. These compounds inhibit the enzymatic breakdown of polysaccharides into absorbable monosaccharides, thereby reducing postprandial glucose levels. Despite their efficacy, conventional AGIs are associated with gastrointestinal side effects, such as flatulence, diarrhea, and abdominal discomfort. These limitations have prompted the search for novel AGIs with enhanced efficacy, reduced side effects, and improved pharmacokinetic profiles [11,12]. The development of new α-glucosidase inhibitors focuses on both natural product-inspired compounds and synthetic derivatives [13,14]. Among these, Schiff base derivatives have gained attention due to their structural versatility and diverse biological activities.

Schiff bases, characterized by the presence of an imine (-C=N-) functional group, are synthesized through the condensation of primary amines with aldehydes or ketones. This structural class has demonstrated a broad spectrum of pharmacological activities, including antimicrobial, antioxidant, anticancer, anti-inflammatory, and enzyme inhibitory properties [15,16]. The versatility of Schiff bases lies in their ability to interact with biological targets through hydrogen bonding, electrostatic interactions, and hydrophobic effects. These features make Schiff bases promising scaffolds for designing novel AGIs, particularly for metabolic enzymes such as α-glucosidase [17–19].

Indole, a bicyclic aromatic heterocycle, is another structural motif with significant pharmacological relevance. Found in a wide range of natural products and synthetic compounds, indole derivatives exhibit a plethora of biological activities, including anti-inflammatory, antimicrobial, anticancer, and antidiabetic effects [20–23]. The indole nucleus's electron-rich nature and planar structure facilitate interactions with biological targets, making it an attractive scaffold for drug discovery. In particular, indole derivatives have shown potential as AGI by forming stable interactions within active sites, often through π-π stacking and hydrogen bonding. Combining the structural attributes of Schiff bases and indole derivatives presents a unique opportunity to develop potent and selective α-glucosidase inhibitors [20,22,24–26].

A closer examination of clinically approved drugs and bioactive natural products reveals that C_5-substitution on the indole ring plays a pivotal role in modulating biological activity, particularly through influences on π-stacking, electron density, and lipophilicity. As shown in Figure 1a, several marketed agents such as indomethacin, [27] delavirdine, [28] sumatriptan, [29] and zafirlukast [30] bear functional groups at the C_5 position, which contribute to their therapeutic efficacy in anti-inflammatory, antiviral, antimigraine, and antiasthmatic applications, respectively. Similarly, naturally occurring compounds like 5-methoxytryptamine [31] and 5-MeO-DMT [32] feature a C_5-methoxy substitution, which enhances receptor binding and CNS permeability.

In contrast, previously reported indole-based hydrazone derivatives with α-glucosidase inhibitory activity often lacked a consistent strategy for substitution at the C_5 position. [33–39] As illustrated in Figure 1b, past efforts employed unsubstituted [33–36] or chloro [37,38]/amido [39]-functionalized indoles without clear structure-guided justification [33–35]. For instance, a 2015 study evaluated unsubstituted indole-3-carbaldehyde hydrazones, which showed moderate enzyme inhibition ($IC_{50} \approx 17.7$ μM), but did not explore scaffold modifications to enhance electronic properties or pharmacokinetics [33]. These analogs demonstrated moderate biological activity but suffered from limited physicochemical optimization. To address this gap, we designed a focused series of C_5-methoxy-substituted indole-based Schiff base derivatives (Figure 1c), aiming to improve electronic distribution, π–π stacking, and lipophilicity, thereby enhancing binding affinity and pharmacokinetic potential.

 doi:10.20944/preprints202508.0415.v1

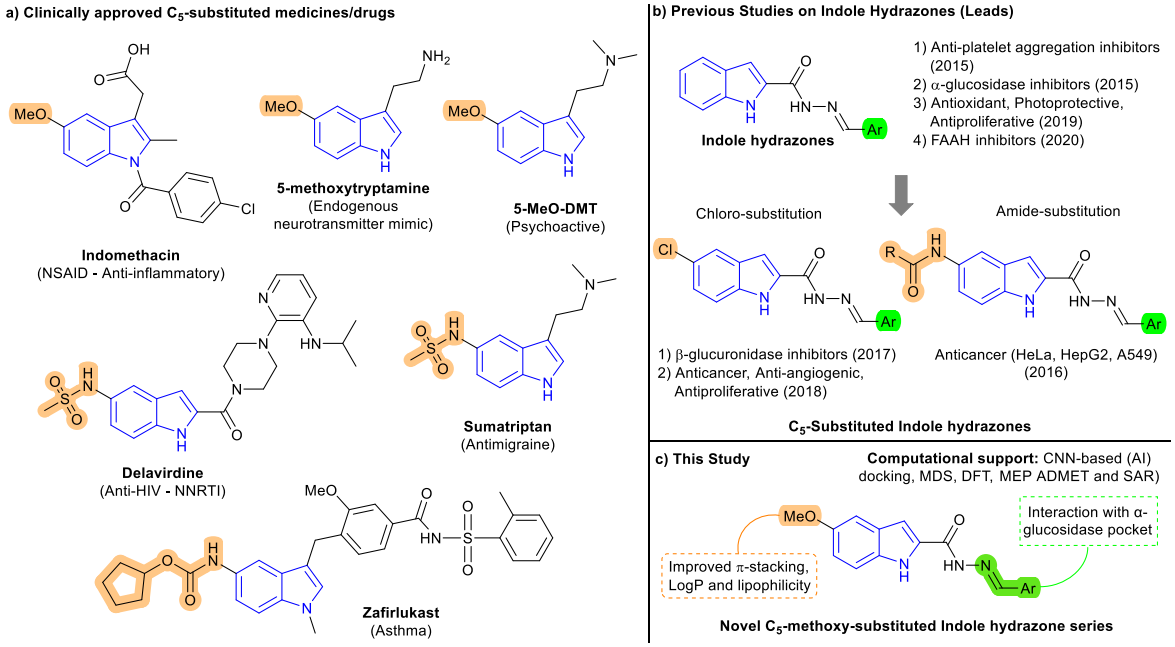

Figure 1. Design evolution of C5-substituted indole-based compounds. (a) Clinically approved indole drugs and natural products featuring C5-substituents, supporting the pharmacological relevance of this position. NSAID = nonsteroidal anti-inflammatory drug; NNRTI = non-nucleoside reverse transcriptase inhibitor; DMT = dimethyltryptamine. (b) Literature examples of indole hydrazones and their bioactivities, including prior leads with C5-chloro or amide modifications. (c) This study: design of C5-methoxy-indole Schiff bases with enhanced π-stacking, lipophilicity, and predicted α-glucosidase affinity supported by CNN-based docking, MD simulation, DFT, MEP, SAR and ADMET profiling.

The synthesized compounds were evaluated for α-glucosidase inhibitory activity and benchmarked against the clinical reference acarbose. To elucidate structure–activity relationships (SARs), we employed a suite of computational tools including Density Functional Theory (DFT), molecular electrostatic potential (MEP) mapping, CNN (Convolutional Neural Network)-based docking, molecular dynamics simulations, and ADMET profiling. This integrated approach enabled mechanistic interpretation of binding interactions and drug-likeness, ultimately contributing to the rational development of optimized α-glucosidase inhibitors for postprandial glycemic control in T2DM.

2. Materials and Methods

2.1. Materials

All chemicals and reagents, including solvents, were purchased from Sigma-Aldrich and were of analytical grade. Ethanol (EtOH, 99.5%) and other solvents used in synthesis were employed without further purification. Glassware was oven-dried prior to use, and reactions were conducted under a dry nitrogen atmosphere unless specified otherwise. Thin-layer chromatography (TLC) was performed using pre-coated silica gel 60 F254 aluminum plates (0.25 mm, E. Merck) and visualized under a UV lamp or after ninhydrin treatment. Column chromatography was carried out with silica gel (100–200 mesh and 230–400 mesh) as the stationary phase, and elution solvents were selected based on TLC mobility.

2.2. Synthesis and Characterization of Schiff Base Derivatives of Indole

The synthetic route (Scheme 1) for the Schiff base derivatives **4a–4j** involved a three-step process as outlined below [33,40].

 doi:10.20944/preprints202508.0415.v1

The synthesized compounds were characterized using a combination of spectroscopic techniques to confirm their structures and purities. The characteristic imine (-C=N-) proton signal was observed in the range of δ 8.25–8.85 ppm in the ^{1}H NMR spectra, while the ^{13}C NMR spectra displayed distinct peaks for the imine carbon at δ 157–163 ppm. High-resolution mass spectrometry (HRMS) analysis provided molecular ion peaks consistent with the expected molecular formulas, further confirming the successful synthesis of the desired compounds. Additional signals corresponding to functional group modifications were observed and analyzed to validate the structural diversity introduced through various aromatic aldehydes.

2.2.1. 5-Methoxy Indole Ester (2)

Indole compound 1 (2 g, 7.57 mmol) was dissolved in 40 mL of ethanol. After stirring at room temperature for 10 minutes, 1 M H_2SO_4 (0.56 mL) was added dropwise. The reaction mixture was refluxed at 90 °C for 18 hours. Upon completion, the reaction was diluted with ethyl acetate (EtOAc, 40 mL) and washed with aqueous $NaHCO_3$. The organic layer was dried over Na_2SO_4, concentrated, and purified via silica gel column chromatography using 10% EtOAc-petroleum ether as the eluent, yielding Indole-ester 2. White solid (1.64 g, 74% yield). ^{1}H NMR (600 MHz, DMSO-d_6): δ 11.74 (s, 1H), 7.35 (d, J = 8.9 Hz, 1H), 7.10 (d, J = 2.4 Hz, 1H), 7.05 (d, J = 2.0 Hz, 1H), 6.92 (dd, J = 8.9, 2.5 Hz, 1H), 4.33 (q, J = 7.1 Hz, 2H), 3.76 (s, 3H), 1.34 (t, J = 7.1 Hz, 3H). ^{13}C NMR (151 MHz, DMSO-d_6): δ 161.73, 154.41, 133.18, 128.00, 127.51, 116.69, 113.94, 107.72, 102.41, 60.78, 55.67, 14.79. HRMS (ESI-TOF) (m/z): $[M + H]^+$ calculated for $C_{12}H_{13}NO_3$ 219.0895; found 219.0891.

2.2.2. 5-Methoxy Indole Hydrazide (3)

Hydrazine hydrate (0.77 mL, 15.41 mmol, 3 equiv.) was added to a solution of compound 2 (1.5 g, 5.13 mmol) in ethanol (37 mL). The mixture was refluxed at 90 °C for 16 hours. After reaction completion, the mixture was poured into crushed ice, and the precipitate was filtered, washed with water, and recrystallized from ethanol to obtain Indole-Hydrazide 3. White solid (1.14 g, 82% yield; ^{1}H NMR (600 MHz, DMSO-d_6): δ 11.43 (s, 1H), 9.72 (s, 1H), 7.31 (d, J = 8.9 Hz, 1H), 7.06 (d, J = 2.5 Hz, 1H), 7.00 (dd, J = 2.3, 0.9 Hz, 1H), 6.82 (dd, J = 8.9, 2.5 Hz, 1H), 4.48 (s, 2H), 3.75 (s, 3H). ^{13}C NMR (151 MHz, DMSO-d_6): δ 161.66, 154.19, 132.04, 131.28, 127.88, 114.69, 113.50, 102.40, 102.07, 55.70. HRMS (ESI-TOF) (m/z): $[M + H]^+$ calculated for $C_{10}H_{11}N_3O_2$ 205.0851; found 205.0844.

2.2.3. Hydrazone Derivatives (4a-j).

Compound **3** (100 mg, 0.48 mmol) was dissolved in 10 mL of 96% ethanol, and the appropriate substituted aromatic aldehyde (0.52 mol) was added. The mixture was refluxed for 3 hours and then cooled to room temperature. After stirring overnight, the precipitated product was filtered, washed, and purified by recrystallization from ethanol. Further purification was achieved using silica gel column chromatography (100-200 mesh, 20% EtOAc-petroleum ether).

(*E*)-5-methoxy-N'-(thiazol-2-ylmethylene)-1*H*-indole-2-carbohydrazide (**4a**) was prepared from using the general procedure, after purification, **4a** was obtained as a white solid (116 mg, 79% yield). ^{1}H NMR (600 MHz, DMSO-d_6): δ 12.15 (s, 2H), 11.74 (s, 2H), 8.70 (s, 2H), 7.99 (d, J = 3.2 Hz, 2H), 7.87 (d, J = 3.2 Hz, 2H), 7.37 (d, J = 8.9 Hz, 2H), 7.25 (s, 2H), 7.16 (d, J = 2.4 Hz, 2H), 6.91 (dd, J = 8.9, 2.5 Hz, 2H). ^{13}C NMR (151 MHz, DMSO-d_6): δ 164.75, 158.10, 154.46, 144.51, 141.49, 133.15, 129.96, 127.59, 122.26, 116.14, 113.80, 104.43, 102.57, 55.77. HRMS (ESI-TOF) (m/z): $[M + H]^+$ calculated for $C_{14}H_{12}N_4O_2S$ 300.3360; found 300.3378.

(*E*)-5-methoxy-N'-(pyridin-3-ylmethylene)-1*H*-indole-2-carbohydrazide (**4b**) was prepared from using the general procedure, after purification, **4b** was obtained as a white solid (116 mg, 81% yield). ^{1}H NMR (600 MHz, DMSO-d_6): δ 12.04 (s, 1H), 11.71 (s, 1H), 8.90 (s, 1H), 8.63 (dd, J = 4.8, 1.7 Hz, 1H), 8.52 (s, 1H), 8.18 (d, J = 8.0 Hz, 1H), 7.55 – 7.49 (m, 1H), 7.37 (d, J = 8.9 Hz, 1H), 7.27 (s, 1H), 7.16 (s, 1H), 6.90 (dd, J = 8.9, 2.5 Hz, 1H), 3.78 (s, 3H). ^{13}C NMR (151 MHz, DMSO-d_6): δ 158.18, 154.40, 151.08,

 doi:10.20944/preprints202508.0415.v1

149.20, 144.69, 133.89, 132.74, 130.78, 130.57, 127.78, 124.51, 115.84, 113.74, 104.04, 102.58, 55.75. HRMS (ESI-TOF) (m/z): $[M + H]^+$ calculated for $C_{16}H_{14}N_4O_2$ 294.3140; found 294.3142.

(*E*)-N'-(4-hydroxybenzylidene)-5-methoxy-1*H*-indole-2-carbohydrazide (**4c**) was prepared from using the general procedure, after purification, **4c** was obtained as a white solid (115 mg, 76% yield). ^{1}H NMR (600 MHz, DMSO-d$_6$): δ 11.68 (s, 1H), 11.65 (s, 1H), 11.58 – 11.38 (m, 1H), 9.96 (s, 1H), 8.36 (s, 1H), 7.59 (d, J = 8.2 Hz, 3H), 7.35 (d, J = 8.9 Hz, 1H), 7.21 (s, 3H), 3.38 (s, 3H). ^{13}C NMR (151 MHz, DMSO-d$_6$): δ 159.84, 157.86, 154.33, 147.82, 132.54, 131.01, 129.30, 127.80, 125.82, 116.19, 115.45, 113.66, 103.41, 102.48, 55.73. HRMS (ESI-TOF) (m/z): $[M + H]^+$ calculated for $C_{17}H_{15}N_3O_3$ 309.3250; found 309.3235.

(*E*)-N'-(4-hydroxy-3-nitrobenzylidene)-5-methoxy-1*H*-indole-2-carbohydrazide (**4d**) was prepared from using the general procedure, after purification, **4d** was obtained as a white solid (142 mg, 82% yield). ^{1}H NMR (600 MHz, DMSO-d$_6$): δ 11.91 (s, 1H), 11.67 (s, 1H), 11.50 (s, 1H), 8.42 (s, 1H), 8.27 – 8.15 (m, 1H), 7.95 (d, J = 8.7 Hz, 1H), 7.36 (d, J = 8.9 Hz, 1H), 7.31 – 7.20 (m, 2H), 7.19 – 7.09 (m, 1H), 6.89 (dd, J = 8.9, 2.4 Hz, 1H), 3.78 (s, 3H). ^{13}C NMR (151 MHz, DMSO-d$_6$): δ 158.06, 154.38, 153.76, 145.37, 137.62, 133.40, 132.67, 130.71, 127.77, 126.34, 124.34, 120.20, 115.69, 113.71, 103.84, 102.55, 55.76. HRMS (ESI-TOF) (m/z): $[M + H]^+$ calculated for $C_{17}H_{14}N_4O_5$ 354.3220; found 354.3211.

(*E*)-N'-(2-hydroxy-4-methoxybenzylidene)-5-methoxy-1*H*-indole-2-carbohydrazide (**4e**) was prepared from using the general procedure, after purification, **4e** was obtained as a white solid (129 mg, 78% yield). ^{1}H NMR (600 MHz, DMSO-d$_6$): δ 12.00 (s, 1H), 11.66 (s, 1H), 11.55 (s, 1H), 8.57 (s, 1H), 7.47 (d, J = 8.5 Hz, 1H), 7.37 (d, J = 8.9 Hz, 1H), 7.22 (s, 1H), 7.15 (d, J = 2.5 Hz, 1H), 6.89 (dd, J = 8.9, 2.4 Hz, 1H), 6.54 (dd, J = 8.6, 2.4 Hz, 1H), 6.51 (d, J = 2.5 Hz, 1H), 3.78 (s, 6H). ^{13}C NMR (151 MHz, DMSO-d$_6$): δ 162.48, 159.72, 157.65, 154.41, 148.28, 132.69, 131.36, 130.46, 127.80, 115.71, 113.72, 112.44, 106.92, 103.78, 102.55, 101.66, 55.78, 55.75. HRMS (ESI-TOF) (m/z): $[M + H]^+$ calculated for $C_{18}H_{17}N_3O_4$ 339.3510; found 339.3524.

(*E*)-N'-(2-fluorobenzylidene)-5-methoxy-1*H*-indole-2-carbohydrazide (**4f**) was prepared from using the general procedure, after purification, **4f** was obtained as a white solid (121 mg, 80% yield). ^{1}H NMR (600 MHz, DMSO-d$_6$): δ 12.00 (s, 1H), 11.71 (s, 1H), 8.72 (s, 1H), 7.99 (t, J = 7.4 Hz, 1H), 7.50 (dd, J = 9.8, 4.0 Hz, 1H), 7.37 (d, J = 9.0 Hz, 1H), 7.34 – 7.30 (m, 2H), 7.26 (s, 1H), 7.16 (s, 1H), 6.90 (dd, J = 8.9, 2.4 Hz, 1H), 3.78 (s, 3H). ^{13}C NMR (151 MHz, DMSO-d$_6$): δ 162.07, 160.41, 158.11, 154.40, 140.06, 132.75, 132.38, 132.32, 130.57, 127.80, 126.78, 125.45, 122.44, 122.37, 116.57, 116.43, 115.84, 113.74, 103.96, 102.58, 55.75. HRMS (ESI-TOF) (m/z): $[M + H]^+$ calculated for $C_{17}H_{14}FN_3O_2$ 311.3164; found 311.3168.

(*E*)-N'-(3-bromobenzylidene)-5-methoxy-1*H*-indole-2-carbohydrazide (**4g**) was prepared from using the general procedure, after purification, compound **4g** was obtained as a white solid (156 mg, 86% yield). ^{1}H NMR (600 MHz, DMSO-d$_6$): δ 12.01 (s, 1H), 11.70 (s, 1H), 8.43 (s, 1H), 7.95 (s, 1H), 7.79 – 7.71 (m, 1H), 7.66 – 7.61 (m, 1H), 7.44 (t, J = 7.8 Hz, 1H), 7.37 (d, J = 8.9 Hz, 1H), 7.26 (s, 1H), 7.18 – 7.11 (m, 1H), 6.90 (dd, J = 8.9, 2.5 Hz, 1H), 3.78 (s, 3H). ^{13}C NMR (151 MHz, DMSO-d$_6$): δ 158.18, 154.39, 145.58, 137.35, 132.95, 132.72, 131.51, 130.57, 129.52, 127.76, 126.68, 122.68, 115.82, 113.74, 104.04, 102.56, 55.76. HRMS (ESI-TOF) (m/z): $[M + H]^+$ calculated for $C_{17}H_{14}BrN_3O_2$ 372.2220; found 372.2231.

(*E*)-5-methoxy-N'-(4-nitrobenzylidene)-1*H*-indole-2-carbohydrazide (**4h**) was prepared from using the general procedure, after purification, **4h** was obtained as a white solid (152 mg, 92% yield). ^{1}H NMR (600 MHz, DMSO-d$_6$): δ 12.17 (s, 1H), 11.74 (s, 1H), 8.56 (s, 1H), 8.33 (d, J = 8.7 Hz, 2H), 8.02 (d, J = 8.5 Hz, 2H), 7.37 (d, J = 8.9 Hz, 1H), 7.28 (s, 1H), 7.17 (s, 1H), 6.91 (dd, J = 8.9, 2.4 Hz, 1H), 3.79 (s, 3H). ^{13}C NMR (151 MHz, DMSO-d$_6$): δ 158.28, 154.42, 148.23, 144.85, 141.21, 132.82, 130.43, 128.42, 127.76, 124.59, 116.03, 113.77, 104.34, 102.59, 55.75. HRMS (ESI-TOF) (m/z): $[M + H]^+$ calculated for $C_{17}H_{14}N_4O_4$ 338.3230; found 338.3232.

(*E*)-5-methoxy-N'-(naphthalen-2-ylmethylene)-1*H*-indole-2-carbohydrazide (**4i**) was prepared from using the general procedure, after purification, **4i** was obtained as a white solid (125 mg, 75% yield). ^{1}H NMR (600 MHz, DMSO-d$_6$): δ 11.99 (s, 1H), 11.73 (s, 1H), 8.64 (s, 1H), 8.18 (s, 1H), 8.07 – 7.90 (m, 4H), 7.62 – 7.52 (m, 2H), 7.39 (d, J = 8.9 Hz, 1H), 7.30 (s, 1H), 7.17 (s, 1H), 6.91 (dd, J = 8.8, 2.4 Hz, 1H), 3.79 (s, 3H). ^{13}C NMR (151 MHz, DMSO-d$_6$): δ 158.16, 154.41, 147.44, 134.18, 133.39, 132.72,

 doi:10.20944/preprints202508.0415.v1

132.62, 130.81, 129.07, 128.98, 128.81, 128.27, 127.82, 127.58, 127.25, 123.23, 115.72, 113.75, 103.90, 102.57, 55.76. HRMS (ESI-TOF) (m/z): $[M + H]^+$ calculated for $C_{21}H_{17}N_3O_2$ 343.3860; found 343.3885.

(*E*)-N'-benzylidene-5-methoxy-1*H*-indole-2-carbohydrazide (**4j**) was prepared from using the general procedure, after purification, **4j** was obtained as a white solid (103 mg, 72% yield). ^{1}H NMR (600 MHz, DMSO-d_6): δ 11.94 (s, 1H), 11.74 (s, 1H), 8.51 (s, 1H), 7.77 (d, J = 7.3 Hz, 2H), 7.47 – 7.41 (m, 4H), 7.31 (s, 1H), 7.16 (s, 1H), 6.92 (dd, J = 8.9, 2.5 Hz, 1H), 3.78 (s, 3H). ^{13}C NMR (151 MHz, DMSO-d_6): δ 158.24, 154.42, 147.55, 134.85, 132.73, 130.79, 130.45, 129.31, 127.85, 127.54, 115.73, 113.76, 103.90, 102.56, 55.72. HRMS (ESI-TOF) (m/z): $[M + H]^+$ calculated for $C_{17}H_{15}N_3O_2$ 293.3260 found 293.3271.

2.3. Biological Assay

The α-glucosidase inhibitory activity of **4a–4j** was evaluated using a standard enzymatic assay. α-Glucosidase from Saccharomyces cerevisiae was employed as the enzyme source, and *p*-nitrophenyl-α-*D*-glucopyranoside (pNPG) served as the substrate. The assay was conducted in a 96-well microplate format at 37 °C in 50 mM phosphate buffer (pH 6.8). Briefly, 10 µL of the test compound (dissolved in DMSO) at various concentrations was mixed with 20 µL of the enzyme solution (1 U/mL) and 50 µL of phosphate buffer. The reaction was initiated by adding 20 µL of pNPG (5 mM), and the mixture was incubated for 30 minutes. The reaction was terminated by adding 50 µL of 0.1 M Na_2CO_3, and the absorbance of the released p-nitrophenol was measured at 450 nm using a microplate reader [33,40].

The percentage inhibition was calculated relative to a negative control, and IC_{50} values for **4g** and **4h** were determined through dose-response analysis. Acarbose was included as the reference standard for comparison. All experiments were performed in triplicate, and the results were expressed as mean ± standard deviation (SD). Statistical significance was evaluated using one-way ANOVA followed by Tukey's post hoc test.

2.4. Theoretical Study

To complement the experimental findings, comprehensive theoretical investigations were carried out to elucidate the electronic, structural, and pharmacokinetic properties of **4a–4j**, as well as their interactions with the α-glucosidase enzyme. The following approaches were employed:

2.4.1. Density Functional Theory (DFT) and Molecular Electrostatic Potential (MEP).

DFT calculations were employed to optimize the geometry and investigate the electronic properties of **4a–4j**. Geometry optimizations were carried out in the gas phase using the ωB97X-D functional and def2-tzvpp basis set [41,42]. Frontier molecular orbitals (FMOs), including the HOMO and LUMO, were analyzed to determine the HOMO-LUMO energy gap (ΔE). MEP maps were generated to visualize charge distributions, highlighting electron-rich regions around carbonyl oxygens and imine nitrogens as potential sites for hydrogen bonding and electrostatic interactions with the enzyme.

2.4.2. Molecular Docking Simulations

The intermolecular interactions were calculated for the indole derivatives and α-glucosidase (α-GLU) binding site. The docking score was average for 10 different conformations of α-GLU with synthesized indole derivatives. The combined Ensemble Docking included 100 ns of molecular dynamics simulation using Amber24 [43] software package. The starting protein coordinates were taken from the crystallographic X-ray structure of human α-GLU in complex with acarbose inhibitor (PDB code: 2QMJ) [44]. The protein was prepared with the Protein Preparation Wizard inside Maestro 2023-4 package, neutralized and salted with 0.1 M NaCl, and included in a 12 Å octahedral water box (8.178 TIP3P explicit water molecules). Docking analysis was performed with the GNINA v1.1 [45] package with a CNN-based scoring function to correct Binding Free Energies. All

 doi:10.20944/preprints202508.0415.v1

calculations were performed with a grid size of 20 × 05 × 20 Å, 128 exhaustiveness value for Monte-Carlo evaluations, and the energy of final binding poses were minimized with 20000 steps.

2.4.3. Molecular Dynamics Simulations (MDS)

were performed to evaluate the stability and interactions of the Schiff base derivatives with the α-glucosidase enzyme active site. Protein-ligand complexes were recovered from GNINA docked complexes, and the simulations were conducted using the Maestro v 2024-3version 13.8.135, MMshare Version 6.4.135, Release 2023-4, and Desmond Multisim v4.0.0 interoperability tools package under the OPLS3 force field. Simulations were carried out for 100 ns in an explicit water environment with periodic boundary conditions under NPT ensemble and 0.02 ps of equation of motion integration. The Root Mean Square Deviations (RMSD) histograms and summary of overall simulation intermolecular interactions were calculated with Desmond tools.

2.4.4. ADMET Profiling, SAR and Statistical Analysis.

The pharmacokinetic and toxicity profiles **4a–4j** were evaluated using ADMETLab v3.0 (https://admetlab3.scbdd.com/server/evaluationCal) [46]. Parameters such as hydrogen bond donors/acceptors, logP, TPSA, and Caco-2 permeability were analyzed to assess drug-likeness. SAR analysis was conducted to identify the molecular features critical for α-glucosidase inhibitory activity. Statistical models were built using Python and R to identify significant trends and validate the experimental findings. All visualizations, including activity-trend plots and SAR correlations, were generated using Python.

2.4.5. Statistical Analysis and Data Visualization

All statistical analyses, including the calculation of IC_{50} values, standard deviations, and significance testing (*p*-values), were performed using Python and R. Data analysis was conducted using one-way ANOVA, followed by Tukey's post-hoc test for multiple comparisons. Detailed statistical analysis is provided in the ESI. All plots were generated using Python to ensure reproducibility and consistency.

3. Results and Discussion

3.1. Synthesis and Characterization

Indole-based Schiff base derivatives **4a–4j** were synthesized via a straightforward three-step process. The starting material, 5-methoxy-1*H*-indole-2-carboxylic acid **1**, was esterified using ethanol and catalytic sulfuric acid to yield ethyl 5-methoxy-1*H*-indole-2-carboxylate **2**. This intermediate was then subjected to hydrazinolysis with hydrazine hydrate under reflux to afford 5-methoxy-1*H*-indole-2-carbohydrazide **3** in high yields. The use of 5-methoxy-1H-indole-2-carboxylic acid as the starting scaffold was a deliberate design choice to incorporate a fixed methoxy group at the C_5 position, aimed at enhancing lipophilicity and π-electron distribution across the indole ring.

The final step involved the condensation of compound **3** with various aromatic aldehydes to yield the corresponding Schiff base derivatives **4a–4j**. The reaction was carried out in ethanol with catalytic acetic acid under reflux, resulting in excellent yields of the desired products. The aromatic aldehyde variations introduced diverse substituents (Ar) into the final products, including thiazole **4a**, pyridine **4b**, 4-hydroxyphenyl **4c**, 3-nitro-4-hydroxyphenyl **4d**, 2-hydroxy-4-methoxyphenyl **4e**, 2-fluorophenyl **4f**, 3-bromophenyl **4g**, 4-nitrophenyl **4h**, naphthalene **4i**, and phenyl **4j** (Scheme 1) [33,40].

The structures of all synthesized compounds were confirmed using spectroscopic techniques, including ^{1}H NMR, ^{13}C NMR, and HRMS. The characteristic imine (-C=N-) proton signal was observed in the range of δ 8.25–8.85 ppm in the ^{1}H NMR spectra, while the ^{13}C NMR spectra showed signals for the imine carbon at δ 157–163 ppm. HRMS analysis provided molecular ion peaks

 doi:10.20944/preprints202508.0415.v1

consistent with the expected molecular formulas, confirming the successful synthesis of the target compounds.

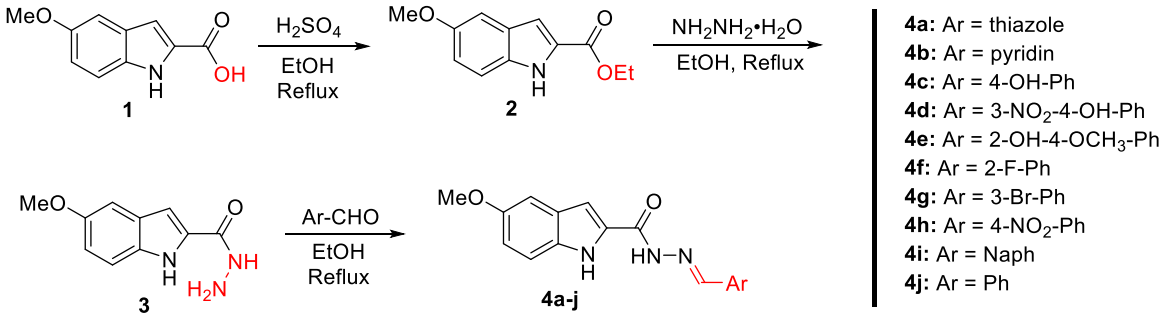

Scheme 1. Synthesis of indole-based Schiff base derivatives **4a–4j** via esterification, hydrazinolysis, and condensation with aromatic aldehydes.

3.2. α-Glucosidase Inhibition Assay

The α-glucosidase inhibitory activity of compounds **4a–4j** was evaluated at a fixed concentration of 100 μM. The results, presented in Table 1, revealed that compounds **4g**, **4h**, **4e**, and **4i** exhibited the highest inhibitory activities, achieving 91.06%, 89.11%, 82.21%, and 82.73% inhibition, respectively. These activities were comparable to or exceeded that of the standard inhibitor, Acarbose (84.66%), indicating the strong potential of these derivatives. In contrast, compounds **4b** and **4d** demonstrated relatively low inhibition values (26.37% and 27.97%, respectively), suggesting weaker interactions with the enzyme's active site. While an overall ANOVA did not indicate a statistically significant difference across all groups ($p = 0.681$), subsequent pairwise comparisons using Tukey's post-hoc test revealed significant differences between individual compounds. Notably, compounds **4g**, **4h**, **4e**, and **4i** showed significantly higher inhibition compared to several other derivatives in the series (Table 1, Figure 2).

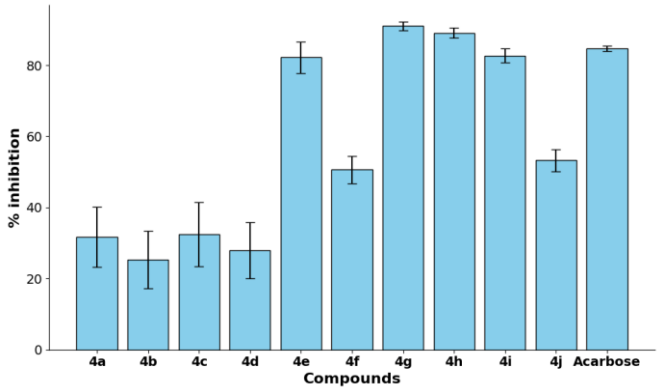

Figure 2. The % inhibition of α-glucosidase activity by compounds **4a–4j** and the standard control Acarbose at a fixed concentration of 100 μM.

Table 1. α-Glucosidase inhibitory activity of compounds **4a–4j** at 100 μM concentration, IC_{50} values, HOMO-LUMO energy gap, binding free energy (BFE), and CNN-based binding affinity (AFF).

Entry	Compounds	Ar	% inhibition [a]	IC_{50} (μM)	ΔE [b] (eV)	BFE [c] (Kcal mol^{-1})	Affinity [d] (pK units)
1	**4a**	thiazole	31.75 ± 8.42	n.d.[e]	6.74	-5.64	5.7
2	**4b**	pyridine	26.37 ± 8.04	n.d.	7.00	-6.26	6.0
3	**4c**	4-OH-Ph	32.51 ± 8.99	n.d.	7.28	-6.64	6.4

 doi:10.20944/preprints202508.0415.v1

4	**4d**	3-NO_2-4-OH-Ph	27.97 ± 7.96	n.d.	6.20	-6.53	6.3
5	**4e**	2-OH-4-OCH_3-Ph	82.21 ± 4.47	16.42 ± 0.08	7.71	-6.37	6.1
6	**4f**	2-F-Ph	50.65 ± 3.86	n.d.	6.96	-6.60	6.5
7	**4g**	3-Br-Ph	91.06 ± 1.25	10.89 ± 0.08	7.01	-6.75	6.6
8	**4h**	4-NO_2-Ph	89.11 ± 1.39	14.53 ± 0.76	6.23	-6.77	6.9
9	**4i**	Naph	82.73 ± 1.90	19.54 ± 1.37	6.99	-6.43	6.2
10	**4j**	Ph	53.23 ± 3.11	n.d.	7.14	-6.20	6.0
11	Acarbose	—	84.66 ± 0.71	48.95 ± 15.98	—	-7.40	7.1

[a] % Inhibition values were calculated based on absorbance at 450 nm at a fixed concentration of 100 μM and converted to % inhibition using the standard formula. [b] ΔE (eV): HOMO-LUMO energy gap calculated at the ωB97X-D/def2-tzvpp level. [c] Binding Free Energy and [d] CNN-based calculated affinity in pK units obtained from molecular dynamic simulations. [e] IC_{50} values not determined.

To further assess the potency of the synthesized compounds, IC_{50} values, representing the concentration required to achieve 50% inhibition, were determined for the most active derivatives (Table 1, Figure S1). Compound **4g** exhibited the highest potency with an IC_{50} value of 10.89 ± 0.08 μM, followed by **4h** (14.53 ± 0.76 μM), **4e** (16.42 ± 0.08 μM), and **4i** (19.54 ± 1.37 μM). In contrast, the reference standard acarbose exhibited an IC_{50} value of 48.95 ± 15.98 μM, demonstrating that **4g**, **4h**, **4e**, and **4i** possess superior inhibitory potency. These results suggest that compounds **4e**, **4g**, **4h**, and **4i** hold significant promise as potent α-glucosidase inhibitors.

3.3. Density Functional Theory (DFT) Study

DFT calculations were performed to investigate the electronic and structural properties of derivatives **4a–4j** [41,42]. Geometry optimizations and conformational analyses revealed the most energetically favorable structures for each derivative. In most cases, a single conformer was significantly more stable, with energy differences exceeding 5 kcal/mol compared to alternative configurations. For instance, intramolecular interactions, such as hydrogen bonding in compound **4e**, were found to stabilize specific conformations, influencing their overall geometry. Planarity was observed in certain derivatives, such as those containing thiazole or fluorine substituents, due to electronic effects and reduced steric repulsion, while non-planarity in others arose from steric clashes between the indole and aromatic rings (Figures S2).

The frontier molecular orbital analysis provided insights into the electronic reactivity of the derivatives. The calculated HOMO-LUMO energy gaps ranged from 6.20 eV for compound **4d** to 7.71 eV for compound **4e**, reflecting variations in electronic stability and reactivity across the series. The analysis revealed that a simple, direct correlation between the energy gap and inhibitory activity was not present. For instance, while the high reactivity predicted by a narrow energy gap for compound **4h** (6.23 eV) corresponded with its strong inhibition (89.11%), this trend did not hold for compound **4d**. Despite having the narrowest energy gap (6.20 eV), **4d** exhibited low inhibitory activity (27.97%). Conversely, some derivatives with wider gaps, such as **4e** (7.71 eV), also demonstrated high inhibitory activity (82.21%), which is likely attributable to other factors like its enhanced conformational stability through intramolecular hydrogen bonding. Furthermore, compound **4g**, which exhibited the highest inhibition of the series (91.06%), possessed an intermediate energy gap of 7.01 eV. These observations suggest that while electronic properties are a contributing factor, the ultimate biological activity is determined by a complex interplay between electronic effects, structural stability, and binding site interactions. Importantly, the fixed methoxy substitution at the C_5 position of the indole ring was found to contribute to consistent HOMO localization across the series, enhancing electron delocalization and potentially influencing π-stacking interactions within the enzyme active site.

 doi:10.20944/preprints202508.0415.v1

The molecular electrostatic potential (MEP) maps further elucidated the electronic distribution across the derivatives. The negative potential regions, primarily located around the carbonyl oxygen and imine nitrogen, indicate their role as hydrogen bond acceptors in enzyme interactions. Compounds with electron-withdrawing groups, such as **4d** and **4h**, exhibited more pronounced negative regions, enhancing their binding affinity through electrostatic interactions. In contrast, electron-donating groups, as seen in **4e**, resulted in more balanced potential distributions, aligning with its high activity. Planar derivatives, such as **4a** and **4f**, demonstrated uniform potential distributions conducive to π-π stacking interactions, while non-planar compounds, such as **4i** and **4j**, showed less symmetry, potentially affecting binding efficiency (ESI, Section 2.3). Notably, the C_5–OMe group contributed to an extended electron cloud on the indole core, which may facilitate interaction with aromatic amino acid residues in the binding site.

3.4. Molecular Docking Calculations

Human α-glucosidase is a critical enzyme that hydrolyzes α-1,4-glycosidic bonds to release glucose from oligosaccharides, and the inhibition of this enzyme represents a strategic therapeutic approach for diabetes mellitus type II management. Molecular docking studies on the crystal structure of the *N*-terminal subunit of human maltase-glucoamylase have shown that the critical intermolecular interactions between inhibitors and the α-GLU active site, such as the catalytic Triad and Nucleophilic Subsite (D542, D327, and D443) are critical for substrate coordination and the subsequent hydrolysis of glycosidic bonds.

Docking analysis showed that the average binding free energy (docking score) of all indole derivatives was slightly higher than that of acarbose co-crystallized drug (-7.40 Kcal mol) (Figure 3) [44,45,47–49]. However, compounds **4g** and **4h** showed average binding free energy (Figure S3) ca. acarbose values (-6.75 and -6.77 Kcal mol, respectively), suggesting that both compounds can interact with the general acid-base residues of the α-GLU substrate active site. The **4g** and **4h** derivatives showed similar interactions as those found on acarbose analogs, suggesting a possible competitive inhibition mechanism. Both compounds were able to establish hydrogen bond interactions with the catalytic aspartate residues in a substrate-like interaction.

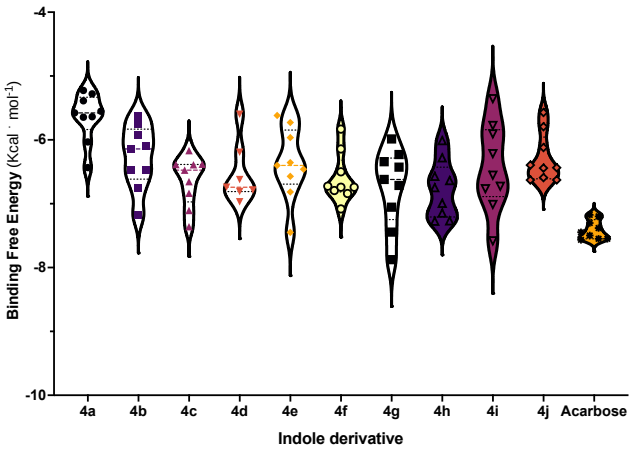

Figure 3. Binding free energies distribution of **4a**-**4j** derivatives, averaged from interactions with the active sites of 10 distinct α-glucosidase conformations.

Moreover, the carbonyl groups of **4g** and **4h** derivatives align with the carboxylate side chains of D542 and D327, disrupting the α-GLU ability to stabilize a transient oxocarbenium if the substrate were present.

Interestingly, 5 Å away from the catalytic triad, the substrate-binding pocket of α-GLU was filled with the Br-phenol and nitro-phenol substituents of **4g** and **4h**, respectively, suggesting that certain features such as aromatic and hydrophobic interactions can stabilize the derivatives binding through

 doi:10.20944/preprints202508.0415.v1

van der Waals forces and π-stacking (W376, F649, and Y1251). For example, inhibitors containing aromatic rings, such as flavonoids or triazole derivatives, exhibit π-π interactions with W376 and F649, anchoring them within the active site [44].

The conserved C_5–methoxy substitution across the series may contribute to consistent positioning and π-electron delocalization of the indole core, facilitating stacking interactions and favorable orientation during binding.

*3.5. Molecular Dynamics Simulation for **4g** and **4h***

To overcome the conformational limitations inherent in static molecular docking, explicit-solvent molecular dynamics simulations (MDS) were performed on the α-glucosidase–ligand complexes of compounds **4g** and **4h**. These simulations provide time-dependent sampling of ligand and protein flexibility, capturing dynamic interactions such as sidechain reorientations, π-stacking stabilization, and hydrogen bond persistence in a physiological aqueous environment. MDS also refines binding predictions by calculating all-atom positions at each integration step, thereby improving the reliability of binding mode assessments.

Three independent replicas of each complex were simulated (3 × 100 ns), and structural stability was assessed using the root-mean-square deviation (RMSD) of the enzyme's α-carbon atoms. Compound **4g** exhibited lower RMSD values than acarbose, with an average of 1.3 Å, while 4h showed RMSD values similar to the standard drug (average 1.8 Å) (Figure 4). These values indicate that both compounds form highly stable enzyme–inhibitor complexes, with 4g showing a slightly more rigid binding mode.

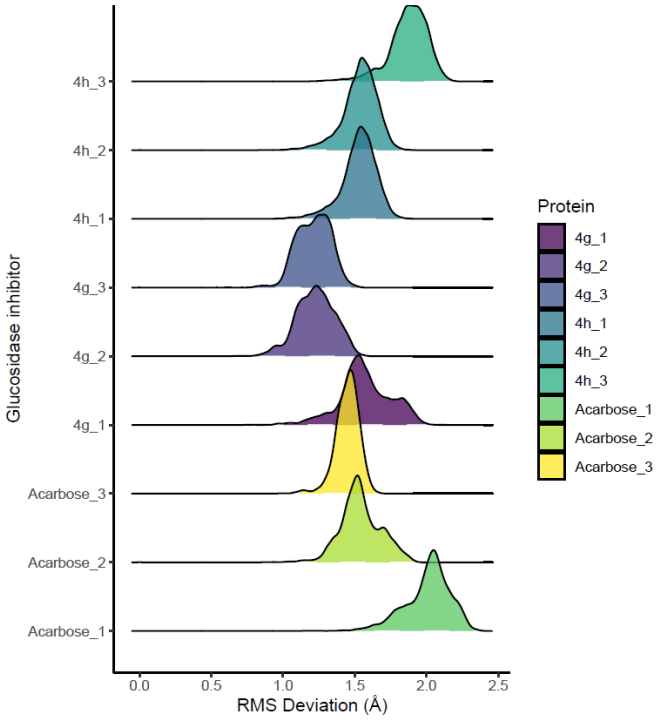

Figure 4. RMSD histograms of the enzyme's alpha-carbon atoms, reflecting conformational equilibration of complexes.

Throughout the simulation period, both **4g** and **4h** maintained strong electrostatic and hydrogen bonding interactions with key catalytic residues D542 and D327. In addition, persistent π–π stacking interactions were observed with aromatic residues W406 and F450, supporting the role of aromatic substituents and the indole core in stabilizing the binding mode (Figure 5). The fixed C_5–methoxy group may contribute to electronic delocalization and planarity of the indole ring, facilitating consistent π-stacking alignment within the enzyme's hydrophobic pocket.

 doi:10.20944/preprints202508.0415.v1

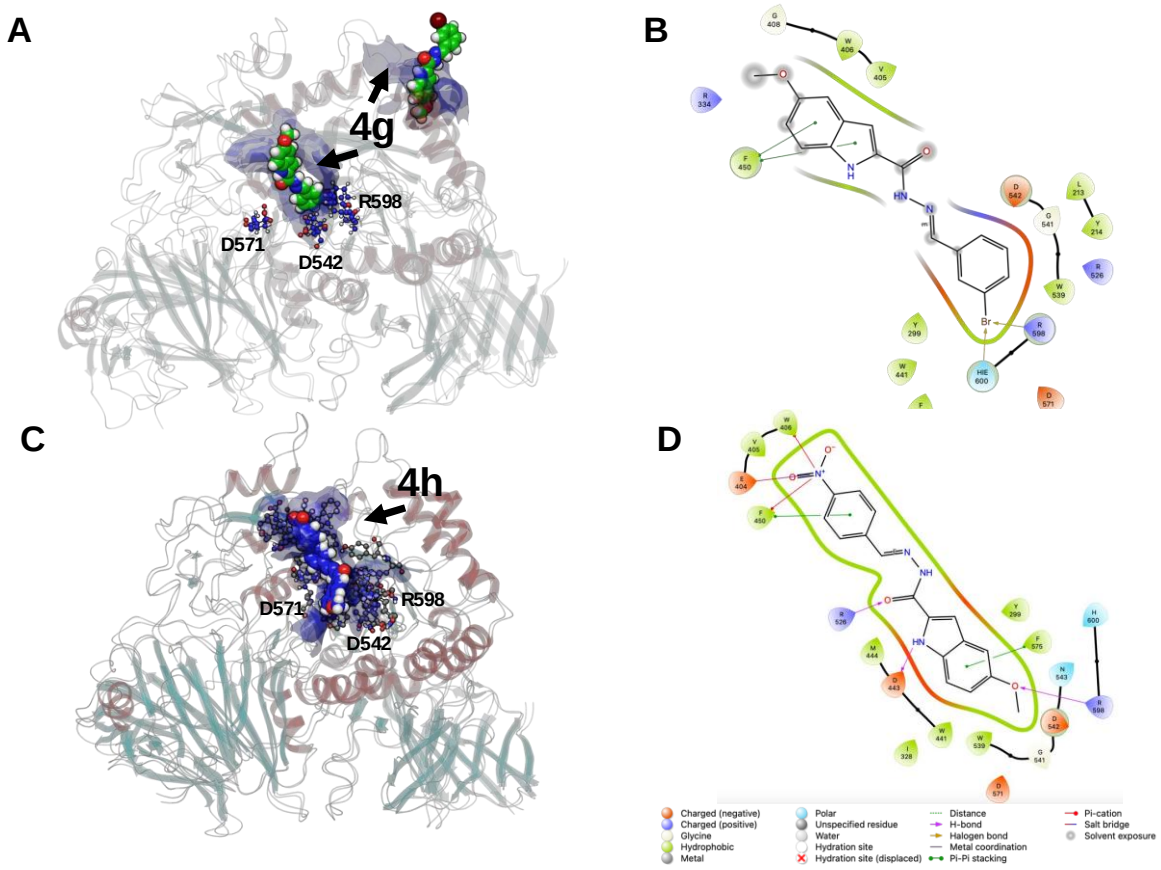

Figure 5. Ligand interaction diagrams of indole derivatives in complex to α-glucosidase binding site. **A**, **B**: 3D and 2D ligand interaction diagram of **4g** derivative. **C**, **D**: 3D and 2D ligand interaction diagram of **4h** derivative. Solvent-Accessible Surface Areas (SASA) of the α-glucosidase binding site are shown as blue surfaces, with intermolecular interactions (H-bonds and π-stacking) depicted as yellow and blue dotted lines, respectively. 2D interaction diagram legends are shown at the bottom of the figure.

*3.6. ADMET Profiling for **4e**, **4g**, **4h**, **4i** and Acarbose*

The ADMET properties of the most active compounds, **4e**, **4g**, **4h**, and **4i** alongside the standard α-glucosidase inhibitor, acarbose, are summarized in Table 2. These parameters offer critical insights into drug-likeness, absorption, distribution, metabolism, excretion, and toxicity

The molecular weights (MW) of the synthesized compounds (338–371 g/mol) fall well within the optimal drug-likeness range of 100–600 g/mol. In contrast, acarbose has a significantly higher MW (645.25 g/mol), which may limit its membrane permeability and bioavailability. The number of hydrogen bond donors (2–3) and acceptors (5–8) in the active compounds also adheres to Lipinski's Rule of Five, unlike acarbose, which possesses an excessive number of both (14 donors, 19 acceptors), contributing to poor pharmacokinetic performance.

The LogP values of the synthesized compounds (2.925–4.126) indicate a favorable balance between hydrophilicity and lipophilicity, essential for membrane permeability and oral absorption. Acarbose, with a LogP of −4.48, is highly hydrophilic, which is consistent with its poor permeability. Topological polar surface area (TPSA) values for **4e**, **4g**, **4h**, and **4i** (66.48–109.62 Å²) support their potential for passive absorption, whereas acarbose exhibits a TPSA of 321.17 Å², well above the threshold typically associated with good intestinal permeability.

 doi:10.20944/preprints202508.0415.v1

Table 2. Evaluated drug-likeness parameters for **4e**, **4g**, **4h**, **4i** and Acarbose.

Parameter [a]	**4e**	**4g**	**4h**	**4i**	**Acarbose**[m]
MW (g/mol) [b]	339.12	371.03	338.1	343.13	645.25
H-donor [c]	3	2	2	2	14
H-acceptor [d]	7	5	8	5	19
LogP [e]	3.184	4.126	2.925	3.845	−4.48
TPSA (Å²) [f]	95.94	66.48	109.62	66.48	321.17
Caco-2 Permeability [g]	−5.394	−5.201	−5.421	−5.282	−7.289
HIA[h]	Low	Low	Low	Low	High
PPB [i]	93.401	98.439	97.463	98.841	15.221
BBB Penetration	Low	Low	Low	Low	Low
CYP Inhibition [k]	CYP3A2,	CYP1A2, CYP2C19,	CYP1A2, CYP2C19,	CYP1A2, CYP2C19,	CYP2C8
hERG Blocker [l]	0.288	0.342	0.44	0.44	0.001
Toxicity	Moderate	Moderate	Moderate	Moderate	Moderate

[a] All ADMET data were obtained from ADMETlab 3.0. [b] Molecular weight (Optimal range: 100–600) [c] H-donor (Optimal range: 0–12) and [d] H-acceptor counts indicate the number of functional groups contributing to hydrogen bonding, influencing solubility and permeability (Optimal range: 0–7). [e] Lipophilicity (Optimal range: 1–5). [f] Topological Polar Surface Area [g] Caco-2 Permeability (Optimal: higher than −5.15 Log unit). [h] Human Intestinal Absorption; Category 1 (HIA+): HIA ≥ 30%; Category 0 (HIA-): HIA < 30%. The output value indicates the probability of being HIA+. [i] Plasma Protein Binding (Optimal: <90%) [j] Blood-Brain Barrier Penetration; BBB+ (Category 1): Penetrates; BBB- (Category 0): Does not penetrate. Output value indicates probability of BBB+. [k] Compound likely inhibits the P450 enzymes. [l] Human Ether Related Gene (indicates cardiotoxicity risk) The output value indicates the probability of being hERG+ (0–1). [m] Standard reference for comparison.

While Caco-2 permeability predictions for all compounds fell below the ideal cutoff (LogP > −5.15), the Human Intestinal Absorption (HIA) score for acarbose (0.998) remains high due to its known transport via carrier-mediated mechanisms. In contrast, the active compounds exhibited low HIA probabilities, likely due to their more lipophilic nature and larger aromatic domains. High plasma protein binding (PPB) values for the active compounds (93.4–98.8%) suggest efficient systemic retention and circulation, while acarbose, with a PPB of only 15.2%, may be cleared more rapidly from systemic circulation.

None of the tested compounds are predicted to penetrate the blood–brain barrier (BBB), which is favorable for minimizing central nervous system side effects. However, all synthesized derivatives are predicted to inhibit cytochrome P450 isoforms CYP2C19 and CYP2C8, with compound **4g** also inhibiting CYP1A2, indicating a potential risk for drug–drug interactions that warrants future investigation.

The predicted probability of hERG inhibition, a marker for cardiotoxicity ranged from 0.288 to 0.440 for the active compounds, classifying them as moderate-risk candidates. In contrast, acarbose displayed a low hERG blocker probability (0.001), indicating minimal cardiotoxicity risk.

Importantly, the fixed methoxy substitution at the C_5 position of the indole scaffold likely contributes to the favorable lipophilicity and moderate TPSA observed across the active series, helping position these compounds within an optimal physicochemical window for oral bioavailability.

 doi:10.20944/preprints202508.0415.v1

3.7. Structure-Activity Relationship (SAR) Analysis

SAR analysis was conducted to evaluate the influence of electronic effects, hydrogen bonding, steric hindrance, and molecular planarity on the α-glucosidase inhibitory activity of compounds **4a–4j**. The goal was to identify key structural features that modulate enzyme binding and inhibition efficiency.

All synthesized derivatives share a fixed methoxy substitution at the C_5 position of the indole core. This design feature was introduced to enhance lipophilicity and π-electron delocalization, providing a consistent electronic and steric platform for exploring the impact of varied aryl substitutions on biological activity.

The analysis revealed that electron-withdrawing groups (EWGs) played a significant role in enhancing binding affinity and enzyme inhibition. Compounds **4g** (bromobenzene, 91.06%) and **4h** (nitrobenzene, 89.11%) exhibited the highest inhibitory activity, which can be attributed to the ability of halogen atoms and nitro groups to facilitate strong electronic interactions and stabilize the enzyme-ligand complex. In contrast, compounds containing weaker EWGs, such as **4a** (thiazole, 31.75%) and **4b** (pyridine, 26.37%), displayed significantly lower inhibition, highlighting the importance of robust electronic effects in improving binding affinity.

The presence of hydrogen bond donors and acceptors was found to influence enzyme binding and inhibition. Compound **4e** (hydroxy-methoxybenzene, 82.21%), which contains both hydroxyl (-OH) and methoxy (-OCH_3) groups, demonstrated strong binding affinity, likely due to its ability to form hydrogen bonds within the active site. In contrast, compounds with limited hydrogen bonding potential, such as **4f** (fluorobenzene, 50.65%), showed moderate inhibitory activity. These results suggest that functional groups capable of hydrogen bonding enhance enzyme interactions, contributing to higher inhibition percentages.

Steric factors also played a role in determining inhibitory potency. Moderate steric bulk, as observed in **4g** and **4e**, facilitated optimal enzyme binding, resulting in high inhibitory activity. However, excessive steric hindrance, such as in **4i** (naphthalene, 82.73%), slightly reduced activity due to potential steric clashes within the enzyme's active site. Conversely, compounds with minimal steric bulk, including **4a** and **4b**, exhibited lower inhibition, indicating weaker enzyme interactions. These findings emphasize the importance of achieving a balanced steric profile for maximal inhibitory efficiency.

Planarity was also identified as a critical determinant of inhibition. Planar compounds, such as **4g** and **4h**, consistently exhibited high inhibitory activity, suggesting that planar structures enhance ligand-enzyme complementarity and promote strong binding interactions. In contrast, non-planar compounds, such as **4a**, displayed reduced inhibition, reinforcing the necessity of molecular planarity for improved activity.

The SAR analysis demonstrated that strong EWGs and functional groups capable of hydrogen bonding significantly enhance α-glucosidase inhibition, while moderate steric bulk and molecular planarity further improve activity.

4. Conclusions

This study demonstrates the rational design and evaluation of C_5-methoxy-substituted indole-based Schiff base derivatives (**4a**-**4j**) as potent α-glucosidase inhibitors for the management of type 2 diabetes mellitus (T2DM). The fixed methoxy group at the C_5 position was strategically introduced to enhance scaffold lipophilicity, electronic delocalization, and π-stacking potential, features that contributed to improved enzyme binding and drug-likeness. Compounds **4g** and **4h** exhibited superior inhibitory activity compared to the standard drug acarbose, supported by mechanistic insights from CNN-based molecular docking, molecular dynamics simulations, and DFT calculations. ADMET profiling indicated favorable pharmacokinetic properties, including high plasma protein binding, optimal lipophilicity, and moderate cardiotoxicity risk. Collectively, these findings provide a strong foundation for the continued development of indole–Schiff base inhibitors;

 doi:10.20944/preprints202508.0415.v1

however, further in vivo and pharmacodynamic investigations are essential to validate their therapeutic potential and clinical applicability.

Supplementary Materials: The following supporting information can be downloaded at: https://www.mdpi.com/article/doi/s1

Author Contributions: Conceptualization: S.V.P. and T.J.P.; Data curation: S.V.P. and T.J.P.; Formal analysis: T.J.P.; Funding acquisition: F.H.-R.; Investigation: S.K.B. , B.K.G. , V.D.B. , I.D.P.L. , E.D.A. , F.H.-R. and T.J.P.; Methodology: S.K.B. , S.V.P. , A.V.L., J.O.C.J.H. , B.K.G. , V.D.B. , F.H.-R. and T.J.P.; Project administration: S.V.P. and T.J.P.; Resources: I.D.P.L. , E.D.A. and F.H.-R.; Software: A.V.L. , J.O.C.J.H. and T.J.P.; Supervision: S.V.P.; Validation: T.J.P.; Visualization: T.J.P.; Writing–original draft: A.V.L. , I.D.P.L. , E.D.A. , F.H.-R. and T.J.P.; Writing – review & editing: T.J.P. All authors have read and agreed to the published version of the manuscript.

Funding: National Supercomputing Center—IPICYT (Instituto Potosino de Investigación Científica y Tecnológica, A.C.) for the computational research [TKII-AMVL001] and supercomputing resources at Miztli [LANCAD-UNAM-DGTIC-347].

Data Availability Statement: No new data was created.

Acknowledgments: Authors thank Dr. Pradeep Chopra and Dr. Geert-Jan Boons (complex carbohydrate research center, University of Georgia, USA) for their assistance with glucosidase inhibition assay. Authors also acknowledge the technical support of Emanuel Villafán in Huitzilin High-Performance Computing at INECOL and Patricia Romero-Arellano for technical support.

Conflicts of Interest: The authors declare no conflicts of interest.

References

1. World Health Organization. Diabetes. Fact Sheet. Published November 2024. Available online: https://www.who.int/news-room/fact-sheets/detail/diabetes (accessed on 31 December 2024).
2. Ratner, R.E. Controlling Postprandial Hyperglycemia. *Am. J. Cardiol.* **2001**, *88*, 26–31. https://doi.org/10.1016/S0002-9149(01)01834-3.
3. International Diabetes Federation. *IDF Diabetes Atlas*, 10th ed.; IDF: Brussels, Belgium, 2021. Available online: https://diabetesatlas.org (accessed on 31 December 2024).
4. International Diabetes Federation. Diabetes Facts and Figures. Published 2024. Available online: https://idf.org (accessed on 31 December 2024).
5. American Diabetes Association Professional Practice Committee. Retinopathy, Neuropathy, and Foot Care: Standards of Medical Care in Diabetes—2022. *Diabetes Care* **2022**, *45*, S185–S194. https://doi.org/10.2337/dc22-S012
6. Citarella, A.; Cavinato, M.; Rosini, E.; Shehi, H.; Ballabio, F.; Camilloni, C.; Fasano, V.; Silvani, A.; Passarella, D.; Pollegioni, L.; Nardini, M. Nicotinic Acid Derivatives as Novel Noncompetitive α-Amylase and α-Glucosidase Inhibitors for Type 2 Diabetes Treatment. *ACS Med. Chem. Lett.* **2024**, *15*, 1474–1481. https://doi.org/10.1021/acsmedchemlett.4c00190
7. Wu, Y.; Liu, C.; Hu, L. Fragment-Based Dynamic Combinatorial Chemistry for Identification of Selective α-Glucosidase Inhibitors. *ACS Med. Chem. Lett.* **2022**, *13*, 1791–1796. https://doi.org/10.1021/acsmedchemlett.2c00405
8. Mwakalukwa, R.; Amen, Y.; Nagata, M.; Shimizu, K. Postprandial Hyperglycemia Lowering Effect of the Isolated Compounds from Olive Mill Wastes – An Inhibitory Activity and Kinetics Studies on α-Glucosidase and α-Amylase Enzymes. *ACS Omega* **2020**, *5*, 20070–20079. https://doi.org/10.1021/acsomega.0c01622
9. Xu, Y.; Xie, L.; Xie, J.; Liu, Y.; Chen, W. Pelargonidin-3-O-Rutinoside as a Novel α-Glucosidase Inhibitor for Improving Postprandial Hyperglycemia. *Chem. Commun.* **2019**, *55*, 39–42. https://doi.org/10.1039/C8CC07985D
10. American Diabetes Association. Postprandial Blood Glucose. *Diabetes Care* **2001**, *24*, 775–778. https://doi.org/10.2337/diacare.24.4.775

 doi:10.20944/preprints202508.0415.v1

11. Kageyama, S.; Nakamichi, N.; Sekino, H.; Nakano, S. Comparison of the Effects of Acarbose and Voglibose in Healthy Subjects. *Clin. Ther.* **1997**, *19*, 720–729. https://doi.org/10.1016/S0149-2918(97)80096-3
12. Hanefeld, M. The Role of Acarbose in the Treatment of Non-Insulin-Dependent Diabetes Mellitus. *J. Diabetes Complicat.* **1998**, *12*, 228–237. https://doi.org/10.1016/S1056-8727(97)00123-2
13. Cai, Y.-S.; Xie, H.-X.; Zhang, J.-H.; Li, Y.; Zhang, J.; Wang, K.-M.; Jiang, C.-S. An Updated Overview of Synthetic α-Glucosidase Inhibitors: Chemistry and Bioactivities. *Curr. Med. Chem.* **2023**, *23*, 2488–2526. https://doi.org/10.2174/0115680266260682230921054652
14. Kashtoh, H.; Baek, K.-H. Recent Updates on Phytoconstituent Alpha-Glucosidase Inhibitors: An Approach towards the Treatment of Type Two Diabetes. *Plants* **2022**, *11*, 2722. https://doi.org/10.3390/plants11202722
15. Thakor, P.M.; Patel, J.D.; Patel, R.J.; Chaki, S.H.; Khimani, A.J.; Vaidya, Y.H.; Chauhan, A.P.; Dholakia, A.B.; Patel, V.C.; Patel, A.J.; Bhavsar, N.H.; Patel, H.V. Exploring New Schiff Bases: Synthesis, Characterization, and Multifaceted Analysis for Biomedical Applications. *ACS Omega* **2024**, *9*, 35431–35448. https://doi.org/10.1021/acsomega.4c02007
16. Harohally, N.V.; Cherita, C.; Bhatt, P.; Appaiah, K.A. Antiaflatoxigenic and Antimicrobial Activities of Schiff Bases of 2-Hydroxy-4-methoxybenzaldehyde, Cinnamaldehyde, and Similar Aldehydes. *J. Agric. Food Chem.* **2017**, *65*, 8773–8778. https://doi.org/10.1021/acs.jafc.7b02576
17. Sarfraz, M.; Ayyaz, M.; Rauf, A.; Yaqoob, A.; Tooba; Ali, M.A.; Siddique, S.A.; Qureshi, A.M.; Sarfraz, M.H.; Aljowaie, R.M.; Almutairi, S.M.; Arshad, M. New Pyrimidinone Bearing Aminomethylenes and Schiff Bases as Potent Antioxidant, Antibacterial, SARS-CoV-2, and COVID-19 Main Protease MPro Inhibitors: Design, Synthesis, Bioactivities, and Computational Studies. *ACS Omega* **2024**, *9*, 25730–25747. https://doi.org/10.1021/acsomega.3c09393
18. Mushtaq, I.; Ahmad, M.; Saleem, M.; Ahmed, A. Pharmaceutical Significance of Schiff Bases: An Overview. *Futur. J. Pharm. Sci.* **2024**, *10*, 16. https://doi.org/10.1186/s43094-024-00594-5
19. Afzal, H.R.; Khan, N.H.; Sultana, K.; Mobashar, A.; Lareb, A.; Khan, A.; Gull, A.; Afzaal, H.; Khan, M.T.; Rizwan, M.; Imran, M. Schiff Bases of Pioglitazone Provide Better Antidiabetic and Potent Antioxidant Effect in a Streptozotocin–Nicotinamide-Induced Diabetic Rodent Model. *ACS Omega* **2021**, *6*, 4470–4479. https://doi.org/10.1021/acsomega.0c06064
20. Mo, X.; Rao, D.P.; Kaur, K.; Hassan, R.; Abdel-Samea, A.S.; Farhan, S.M.; Bräse, S.; Hashem, H. Indole Derivatives: A Versatile Scaffold in Modern Drug Discovery—An Updated Review on Their Multifaceted Therapeutic Applications (2020–2024). *Molecules* **2024**, *29*, 4770. https://doi.org/10.3390/molecules29194770
21. Puri, S.; Stefan, K.; Khan, S.L.; Pahnke, J.; Stefan, S.M.; Juvale, K. Indole Derivatives as New Structural Class of Potent and Antiproliferative Inhibitors of Monocarboxylate Transporter 1 (MCT1; SLC16A1). *J. Med. Chem.* **2023**, *66*, 657–676. https://doi.org/10.1021/acs.jmedchem.2c01612
22. Mahmoud, E.; Abdelhamid, D.; Youssif, B.G.M.; Gomaa, H.A.M.; Hayallah, A.M.; Abdel-Aziz, M. Design, Synthesis, and Antiproliferative Activity of New Indole/1,2,4-Triazole/Chalcone Hybrids as EGFR and/or c-MET Inhibitors. *Arch. Pharm.* **2024**, *357*, e2300562. https://doi.org/10.1002/ardp.202300562
23. Al-Humaidi, J.Y.; Gomha, S.M.; Riyadh, S.M.; Ibrahim, M.S.; Zaki, M.E.A.; Abolibda, T.Z.; Jefri, O.A.; Abouzied, A.S. Synthesis, Biological Evaluation, and Molecular Docking of Novel Azolylhydrazonothiazoles as Potential Anticancer Agents. *ACS Omega* **2023**, *8*, 34044–34058. https://doi.org/10.1021/acsomega.3c05038
24. Zhang, C.; Xu, D.; Wang, J.; Kang, C. Efficient Synthesis and Biological Activity of Novel Indole Derivatives as VEGFR-2 Tyrosine Kinase Inhibitors. *Russ. J. Gen. Chem.* **2017**, *87*, 3006–3016. https://doi.org/10.1134/S1070363217120465
25. Bang, E.J.; Ra, J.; Choi, H.Y.; Ko, H.M. Synthesis of Benzazepinoindole Derivatives via a One-Pot Process of $TiCl_4$-Catalyzed Indole Alkylation/Pictet-Spengler Cyclization. *Asian J. Org. Chem.* **2022**, *11*, e202100645. https://doi.org/10.1002/ajoc.202100645
26. Duan, S.-F.; Song, L.; Guo, H.-Y.; Deng, H.; Huang, X.; Shen, Q.-K.; Quan, Z.-S.; Yin, X.-M. Research Status of Indole-Modified Natural Products. *RSC Med. Chem.* **2023**, *14*, 2535–2563. https://doi.org/10.1039/D3MD00560G
27. Shen, T.Y. The Discovery of Indomethacin and the Proliferation of NSAIDs. *Semin. Arthritis Rheum.* **1982**, *12*, 89–93. https://doi.org/10.1016/0049-0172(82)90004-X

 doi:10.20944/preprints202508.0415.v1

28. Morse, G.D.; Fischl, M.A.; Shelton, M.J.; Cox, S.R.; Driver, M.; DeRemer, M.; Freimuth, W.W. Single-Dose Pharmacokinetics of Delavirdine Mesylate and Didanosine in Patients with Human Immunodeficiency Virus Infection. *Antimicrob. Agents Chemother.* **1997**, *41*, 169–174. https://doi.org/10.1128/AAC.41.1.169
29. Tansey, M.J.; Pilgrim, A.J.; Lloyd, K. Sumatriptan in the Acute Treatment of Migraine. *J. Neurol. Sci.* **1993**, *114*, 109–116. https://doi.org/10.1016/0022-510x(93)90057-6
30. Dekhuijzen, P.N.; Koopmans, P.P. Pharmacokinetic Profile of Zafirlukast. *Clin. Pharmacokinet.* **2002**, *41*, 105–114. https://doi.org/10.2165/00003088-200241020-00003
31. Tuladhar, B.R.; Costall, B.; Naylor, R.J. Pharmacological Characterization of the 5-Hydroxytryptamine Receptor Mediating Relaxation in the Rat Isolated Ileum. *Br. J. Pharmacol.* **1996**, *119*, 303–310. https://doi.org/10.1111/j.1476-5381.1996.tb15986.x
32. Reckweg, J.T.; Uthaug, M.V.; Szabo, A.; et al. The Clinical Pharmacology and Potential Therapeutic Applications of 5-Methoxy-N,N-dimethyltryptamine (5-MeO-DMT). *J. Neurochem.* **2022**, *162*, 128–146. https://doi.org/10.1111/jnc.15587
33. Taha, M.; Ismail, N.H.; Javaid, K.; Imran, S.; Anouar, E.H.; Wadood, A.; Wahab, A.; Ali, M.; Khan, K.M.; Saad, S.M.; Rahim, F.; Choudhary, M.I. Evaluation of 2-Indolcarbohydrazones as Potent α-Glucosidase Inhibitors, in Silico Studies and DFT-Based Stereochemical Predictions. *Bioorg. Chem.* **2015**, *63*, 24–35. https://doi.org/10.1016/j.bioorg.2015.09.001
34. Mirfazli, S.S.; Khoshneviszadeh, M.; Jeiroudi, M.; Foroumadi, A.; Kobarfard, F.; Shafiee, A. Design, Synthesis and QSAR Study of Arylidene Indoles as Anti-platelet Aggregation Inhibitors. *Med. Chem. Res.* **2016**, *25*, 1–18. https://doi.org/10.1007/s00044-015-1440-7
35. Shang, Y.; Hao, Q.; Jiang, K.; He, M.; Wang, J. Discovery of Heterocyclic Carbohydrazide Derivatives as Novel Selective Fatty Acid Amide Hydrolase Inhibitors: Design, Synthesis and Anti-neuroinflammatory Evaluation. *Bioorg. Med. Chem. Lett.* **2020**, *30*, 127118. https://doi.org/10.1016/j.bmcl.2020.127118
36. Demurtas, M.; Baldisserotto, A.; Lampronti, I.; Moi, D.; Balboni, G.; Pacifico, S.; Vertuani, S.; Manfredini, S.; Onnis, V. Indole Derivatives as Multifunctional Drugs: Synthesis and Evaluation of Antioxidant, Photoprotective and Antiproliferative Activity of Indole Hydrazones. *Bioorg. Chem.* **2019**, *85*, 568–576. https://doi.org/10.1016/j.bioorg.2019.02.007
37. Baharudin, M.S.; Taha, M.; Imran, S.; Ismail, N.H.; Rahim, F.; Javid, M.T.; Khan, K.M.; Ali, M. Synthesis of Indole Analogs as Potent β-Glucuronidase Inhibitors. *Bioorg. Chem.* **2017**, *72*, 323–332. https://doi.org/10.1016/j.bioorg.2017.05.005
38. Zhang, J.; Liu, T.; Chen, M.; Liu, F.; Liu, X.; Zhang, J.; Lin, J.; Jin, Y. Synthesis and Biological Evaluation of Indole-2-carbohydrazide Derivatives as Anticancer Agents with Anti-angiogenic and Antiproliferative Activities. *ChemMedChem* **2018**, *13*, 1181–1192. https://doi.org/10.1002/cmdc.201800033
39. Hu, H.; Wu, J.; Ao, M.; Wang, H.; Zhou, T.; Xue, Y.; Qiu, Y.; Fang, M.; Wu, Z. Synthesis, Structure–Activity Relationship Studies and Biological Evaluation of Novel 2,5-Disubstituted Indole Derivatives as Anticancer Agents. *Chem. Biol. Drug Des.* **2016**, *88*, 766–778. https://doi.org/10.1111/cbdd.12808
40. Bhagwat, S.K.; Hernandez-Rosas, F.; Vidal-Limon, A.; Jimenez-Halla, J.O.C.; Ghotekar, B.K.; Bobade, V.D.; Delgado-Alvarado, E.; Patil, S.V.; Pawar, T.J. Iodinated Salicylhydrazone Derivatives as Potent α-Glucosidase Inhibitors: Synthesis, Enzymatic Activity, Molecular Modeling, and ADMET Profiling. *Chemistry* **2025**, *7*, 117. https://doi.org/10.3390/chemistry7040117
41. Weigend, F.; Ahlrichs, R. Balanced Basis Sets of Split Valence, Triple Zeta Valence and Quadruple Zeta Valence Quality for H to Rn: Design and Assessment of Accuracy. *Phys. Chem. Chem. Phys.* **2005**, *7*, 3297–3305. https://doi.org/10.1039/b508541a
42. Chai, J.-D.; Head-Gordon, M. Long-Range Corrected Hybrid Density Functionals with Damped Atom–Atom Dispersion Corrections. *Phys. Chem. Chem. Phys.* **2008**, *10*, 6615–6620. https://doi.org/10.1039/b810189b
43. Case, D.A.; Aktulga, H.M.; Belfon, K.; Ben-Shalom, I.Y.; Berryman, J.T.; Brozell, S.R.; Cerutti, D.S.; Cheatham, T.E. III; Cisneros, G.A.; Cruzeiro, V.W.D.; Darden, T.A.; Forouzesh, N.; Ghazimirsaeed, M.; Giambaşu, G.; Giese, T.; Gilson, M.K.; Gohlke, H.; Goetz, A.W.; Harris, J.; Huang, Z.; Izadi, S.; Izmailov, S.A.; Kasavajhala, K.; Kaymak, M.C.; Kovalenko, A.; Kurtzman, T.; Lee, T.S.; Li, P.; Li, Z.; Lin, C.; Liu, J.; Luchko, T.; Luo, R.; Machado, M.; Manathunga, M.; Merz, K.M.; Miao, Y.; Mikhailovskii, O.; Monard, G.;

 doi:10.20944/preprints202508.0415.v1

Nguyen, H.; O'Hearn, K.A.; Onufriev, A.; Pan, F.; Pantano, S.; Rahnamoun, A.; Roe, D.R.; Roitberg, A.; Sagui, C.; Schott-Verdugo, S.; Shajan, A.; Shen, J.; Simmerling, C.L.; Skrynnikov, N.R.; Smith, J.; Swails, J.; Walker, R.C.; Wang, J.; Wang, J.; Wu, X.; Wu, Y.; Xiong, Y.; Xue, Y.; York, D.M.; Zhao, C.; Zhu, Q.; Kollman, P.A. *Amber 2024*; University of California: San Francisco, CA, USA, 2024

44. Sim, L.; Quezada-Calvillo, R.; Sterchi, E.E.; Nichols, B.L.; Rose, D.R. Human Intestinal Maltase–Glucoamylase: Crystal Structure of the N-Terminal Catalytic Subunit and Basis of Inhibition and Substrate Specificity. *J. Mol. Biol.* **2008**, *375*, 782-792. https://doi.org/10.1016/j.jmb.2007.10.069
45. McNutt, A.T.; Francoeur, P.; Aggarwal, R.; Masuda, T.; Meli, R.; Ragoza, M.; Sunseri, J.; Koes, D.R. GNINA 1.0: Molecular Docking with Deep Learning. *J. Cheminf.* **2021**, *13*, 43. https://doi.org/10.1186/s13321-021-00522-2
46. Xiong, G.; Wu, Z.; Yi, J.; Fu, L.; Yang, Z.; Hsieh, C.; Yin, M.; Zeng, X.; Wu, C.; Chen, X.; Hou, T.; Cao, D. ADMETlab 2.0: An Integrated Online Platform for Accurate and Comprehensive Predictions of ADMET Properties. *Nucleic Acids Res.* **2021**, *49*, W5–W14. https://doi.org/10.1093/nar/gkab255
47. Olsson, M.H.M.; Søndergaard, C.R.; Rostkowski, M.; Jensen, J.H. PROPKA3: Consistent Treatment of Internal and Surface Residues in Empirical pKa Predictions. *J. Chem. Theory Comput.* **2011**, *7*, 525–537. https://doi.org/10.1021/ct100578z
48. Jorgensen, W.L.; Maxwell, D.S.; Tirado-Rives, J. Development and Testing of the OPLS All-Atom Force Field on Conformational Energetics and Properties of Organic Liquids. *J. Am. Chem. Soc.* **1996**, *118*, 11225–11236. https://doi.org/10.1021/ja9621760
49. Quiroga, R.; Villarreal, M.A. Vinardo: A Scoring Function Based on Autodock Vina Improves Scoring, Docking, and Virtual Screening. *PLoS One* **2016**, *11*, e0155183. https://doi.org/10.1371/journal.pone.0155183